electronic materials

Article

Chlorine Adsorption on TiO_2(110)/Water Interface: Nonadiabatic Molecular Dynamics Simulations for Photocatalytic Water Splitting

Yin-Pai Lin [1], Dmitry Bocharov [1,2], Inta Isakoviča [1], Vladimir Pankratov [1], Aleksandr A. Popov [1], Anatoli I. Popov [1,*] and Sergei Piskunov [1,*]

[1] Institute of Solid State Physics, University of Latvia, 8 Kengaraga str., LV-1063 Riga, Latvia
[2] Transport and Telecommunication Institute, LV-1019 Riga, Latvia
* Correspondence: anatoli.popov@cfi.lu.lv (A.I.P.); piskunov@cfi.lu.lv (S.P.)

Abstract: Chloride is one of the most abundant ions in sea water, which is more available than fresh water. Due to lack of H_2O adsorbate states near the valence band maximum (VBM) edge, the difficulty of water dissociation incidents has been reported on the rutile TiO_2 surface as the excitation energy is around the band gap energy of TiO_2. It is interesting whether the extra chloride can be a benefit to the water dissociation or not. In this study, the models of chlorine adatoms placed on the rutile TiO_2 (110)/water interface are constructed using ab initio methods. The time-dependent spatial charges, bond-lengths of water molecules, and Hirshfeld charges are calculated by real-time time-dependent density functional theory and the Ehrenfest dynamics theory for investigating the excited state nonadiabatic dynamics of water dissociation. This study presents two photoinduced water-splitting pathways related to chlorine and analyzes the photogenerated hole along the reactions. The first step of water dissociation relies on the localized competition of oxygen charges between the dissociated water and the bridge site of TiO_2 for transforming the water into hydroxyl and hydrogen by photoinduced driving force.

Keywords: TiO_2; photocatalyst; seawater; time-dependent density functional theory; Ehrenfest dynamics

Citation: Lin, Y.-P.; Bocharov, D.; Isakoviča, I.; Pankratov V.; Popov, A.A.; Popov, A.I.; Piskunov, S. Chlorine Adsorption on TiO_2(110)/Water Interface: Nonadiabatic Molecular Dynamics Simulations for Photocatalytic Water Splitting. *Electron. Mater.* **2023**, *4*, 33–48. https://doi.org/10.3390/electronicmat4010004

Academic Editor: Wojciech Pisula

Received: 31 December 2022
Revised: 24 February 2023
Accepted: 27 February 2023
Published: 7 March 2023

1. Introduction

The mechanism of photocatalytic water splitting has been extensively studied for pure water [1], but due to the limited availability of freshwater, there has been increased focus on applying similar mechanisms to seawater, which contains up to 96.5% of global water resources [2,3]. The most abundant ion in seawater is Cl^- [1,3], which can be oxidized in a reaction competing with the oxygen evolution reaction. Even now, the perspective has not been determined as uniformed with regards to whether the effect of chlorine is positive or negative on photocatalytic seawater splitting [1]. One viewpoint is that chlorine may promote photogenerated electron-hole recombination and reduce photocatalytic activity [4]. Furthermore, chlorine ions may react with hydroxyl groups on the surface [5]. On the other hand, another viewpoint is that a lack of sufficient kinetic energy may prevent oxidation, and Cl^- may not be oxidized during the reaction [6]. Additionally, photogenerated holes may be eliminated by participating in the Cl^- oxidation reaction, thereby reducing the electron-hole recombination rate [7].

Photoinduced configurations play an important role in triggering water splitting. Currently, the most well suited model catalyst for photocatalytic research is TiO_2 [8–13]. Its widespread use was facilitated by (i) high photocatalytic activity at an incident photon wavelength of $300 < \lambda < 390$ nm and (ii) multifaceted functional properties, such as chemical and thermal stability, as well as attractive mechanical properties [13]. The first step of water disso-

ciation on the rutile TiO_2(110) is attributed to the O–H bond-breaking of water by Equation (1). Generally, this mechanism has been reported previously in the literature [14–18],

$$Ti_{cus} + H_2O + O_{bridge} \rightarrow Ti_{cus}OH + O_{bridge}H, \quad (1)$$

the coordinatively unsaturated sites (cus) and bridge sites are on the surface of TiO_2. According to ab initio molecular dynamics (AIMD) reported by Agosta et al. [16], the hydronium (H_3O^+) is another key intermediate state in the reaction. Specifically, the dissociation of fully hydrated surfaces (wet surfaces) does not occur directly as described by Equation (1). The second water molecule participates in the reaction [16,19] by forming a hydrogen bond with O_{bridge}.

$$\begin{aligned} Ti_{cus} + H_2O + O_{bridge} &\rightarrow Ti_{cus}OH^- + O_{bridge} + H_3O^+ \\ &\rightarrow Ti_{cus}OH + O_{bridge}H + H_2O. \end{aligned} \quad (2)$$

An effective approach to investigate the photoinduced charge transfer in materials relies on the electronic structure within density functional theory (DFT) and especially its dynamics within time-dependent DFT (TDDFT) [17,20–26]. Real-time propagation of TDDFT within Ehrenfest dynamics (ED–TDDFT) are used to approach the non-adiabatic molecule dynamics with photoexcitation to interpret the electron–ion system [17,20–22]. The propagation of the electronic system is based on the time-dependent Kohn–Sham equation with semi-implicit Crank–Nicholson (SICN) method; the algorithm of Velocity Verlet is utilized to manage nuclei propagation for the ionic system. The practical realization of ED–TDDFT in GPAW can be found elsewhere [20,21,27]. Tritsaris et al. [17] used theoretical prediction based on the molecular dynamics, Δ self-consistent field method (Δscf) [28,29], and ED–TDDFT [20,21] to study the photoexcited water dissociation and charge transfer of single water on the rutile (110) according to the Equation (1). Although the doping or defect modifications of TiO_2 can still activate the water-splitting in both experiments [30] that agree with the theoretical predictions [17], the relatively wide band gap of TiO_2 still presents a challenge for water dissociation with photon energy in the visible light region.

This paper aims to focus on the effect of Cl adatoms on water dissociation under photoexcitation. The procedures are summarized in the following steps: *(i)* the initial surface models are undergone by AIMD to let the catalytic systems achieve the designated temperature; *(ii)* the bond lengths of hydroxyl are analyzed to assess the impact of single Cl adatoms on water dissociation; *(iii)* from the literature, it is known that rutile (110) crystallographic plane would not trigger the water dissociation when the excitation energy overcame the band gap of material [17]. It is also worth noting that geometric structures have an influence on the electronic structures and band gap. Besides, there are also many possible new intermediates, such as Cl–O, Cl–H, Cl–O–H, and so on after considering the structure optimization and molecule dynamics. To simplify the models, the cases which almost fulfill the reactions of Equations (1) or (2) are further performed by ED–TDDFT within excited state calculations after AIMD. The excitation energy is limited to the energy near the edge of the visible-light to UV regions, corresponding to the band gap of TiO_2. It should be noted that predicting the impact of chlorine on the band gap and new possible intermediates is beyond the scope of this study.

2. Computational Methods and Models

2.1. Methodology

All simulations were performed by the atomic simulation environment (ASE) [31,32] and the density functional theory (DFT) code GPAW [33,34] based on the projector-augmented wave method. The electronic configurations of valence electrons per atom were as follows: Ti($3s^2 3p^6 3d^2 4s^2$), Cl($3s^2 3p^5$), O($2s^2 2p^4$), and H($1s^1$). The geometry of the system was fully optimized through the use of the Broyden-Fletcher-Goldfarb-Shanno (BFGS) algorithm [31,35]. The optimization process involved relaxing the system until the maximum force of atomic

interactions was below 0.05 eV/Å. During the relaxation of the systems, the Monkhorst-Pack k-point grids with $4 \times 4 \times 4$ (bulk) and $3 \times 2 \times 1$ (TiO_2 surface models) were used to sample the Brillouin zone. The Kohn-Sham wave functions, which consist of a linear combination of atomic orbitals (LCAO) [36], were obtained for structure optimization and AIMD. The finite difference (FD) approach was applied to expand the wave functions on a real space grid for the ED-TDDFT calculations [20,21,27] within the framework of excited state DFT. In order to reduce computational costs, a real-space grid with spacings of 0.2 Å and 0.3 Å were used for the LCAO and FD modes, respectively.

In AIMD calculations, the initial velocities based on the equilibrium of Boltzmann–Maxwell distribution were assigned to the TiO_2 surface models corresponding to temperature increase from 0 K up to 300 K. AIMD simulations were performed on each TiO_2 surface model using a microcanonical ensemble (with constants N, V, and E), and all atoms were fully movable. Each simulation consisted of 300 time steps, each of 1 femtosecond (fs), for a total of 300 fs. The main purpose of these AIMD simulations was to obtain possible equilibrated structures for using in subsequent ED–TDDFT calculations [17,20–22] Then, the equilibrated configurations from these calculations were analyzed to detect the water dissociation. In the literature [16,37], the bond length cutoff R^{C}_{O-H} = 1.3 Å was chosen to determine whether the bond lengths of oxygen-to-hydrogen (d_{O-H}) were broken. This work adopts the same distance of 1.3 Å as the criteria for a broken d_{O-H}. Although this approach is not suitable for a detailed analysis of the real complex reaction [16], it provides a quick and intuitive observation of water dissociation in the abundant trajectories of AIMD simulations.

After molecule dynamics runs, those cases being not fully water-dissociated and following reactions described by Equations (1) or (2) were further considered for simulating the photoexcitation process. For ED–TDDFT calculations, there were two steps used. Firstly, the computational strategy was adopted to describe the moment of vertical excitation within time-independent DFT. The electronic structures of the excited states were obtained by stimulating the designed valence band (VB) electron to the conduction band minimum (CBM) based on the maximum overlap method (MOM). Compared to the Δscf method, MOM is a substitute solution to improve the convergence and avoid the variational collapse to lower energy [38,39]. In this method, one sets the occupancy of -1 for designed VB (hole) and the occupancy of +1 for CBM (electron). The excitation energy was estimated as the energy difference between the designed VB and CBM. Secondly, the excited Kohn–Sham wave functions from MOM were propagated by the ED–TDDFT approach. According to the results published in the literature [17], there were no bond-breaking observations at low-energy (3.93 eV) excitation energy for the single H_2O adsorbate on the rutile (110) TiO_2 surface during 30 fs.It is interesting whether the extra chlorine atom could be used to improve these circumstances for realizing water splitting or not. Therefore, the propagated time was set to maximal 600 time–steps of 0.05 fs within 30 fs summation. The mechanism of charge transfer during dissociation was realized by calculating the charge density differences between excited states and ground states (Δn_{ex-gs}) with the same configurations at each time-step. The purpose of Δn_{ex-gs} is to illustrate the difference between the light-driven and non-light-driven situations along the reaction pathways.

The Perdew–Burke–Ernzerh (PBE) exchange-correlation (XC) functional [40] with consideration of generalized gradient approach (GGA) was utilized for all calculations in the present work. Due to the insufficient prediction of Coulomb interactions on the d-orbitals of titanium, the band gap of TiO_2 would be underestimated by PBE functional with a typical DFT process. By modifying the screened Coulomb interaction of localized d-orbitals, the DFT+U approach improved the electronic structure of TiO_2 within adding an effective $U_{Ti(d)}$ [17,22,41–43]. In the literature [16,37], the prediction of the R^{C}_{O-H} was based on the AIMD applied to GGA XC functional without DFT+U. Although the calculated lattice parameters between DFT and DFT+U changed by less than 1% for TiO_2 [17], the varying distance between the hydroxyl and oxygen adsorbates on the TiO_2 rutile (110) surface cannot be neglected with the DFT+U [44]. In the supplementary S1, the AIMDs with and without DFT+U were discussed, and the DFT+U actually affected the bond lengths.

Therefore, the DFT+U would not perform the simulations for the procedure of structure optimization and AIMD. During excited state time-dependent density functional theory (TDDFT) calculations, the reciprocal space was sampled only at the Gamma point. In order to predict the formation of the polarons for rutile TiO_2 [17,42,45], the DFT+U or other high level XC functional must be thoroughly considered. Therefore, an effective $U_{Ti(d)}$ was applied to improve the electronic structures for describing the electron–ion systems. With respect to FD mode, the band gaps of rutile (110) TiO_2 surface with $U_{Ti(d)}$ = 4.2 eV were, respectively, 2.78 eV for spacing of 0.2 Å and 2.65 eV for spacing of 0.3 Å. LCAO mode predicted that the band gap with $U_{Ti(d)}$ = 4.2 eV was 2.34 eV in agreement with the references [17]. In general, FD mode predicted a better description of electronic structures. The VESTA software was used to visualize the isosurface of Δn_{ex-gs} and atomic environments, while the Python packages NumPy [46] and Matplotlib [47] were used for data analysis and figure producing.

2.2. TiO_2 Surface Models

The detailed illustrations of geometric structures used in this study are shown in Figure 1. To construct the catalytic systems for Cl/H_2O/slab surface models, there were three systems observed, including rutile (110) TiO_2 slab, water adsorbate bonded to Ti atoms, and single Cl adatom deposited on the surface. Initially, the rutile (110) surface was built up with supercells containing 96 atoms (32 Ti atoms, 64 O atoms, and four Ti layers in the z-direction, as shown in Figure 1a). The supercell was cut along the (110) Miller index of the optimized bulk rutile TiO_2. A unit cell consisting of two titanium and four oxygen atoms was used to assemble the bulk rutile TiO2. The optimized lattice parameters of bulk TiO_2 were $a_0 = b_0$ = 4.647 Å, c_0 = 2.969 Å, and d_{Ti-O} = 1.987 Å, which are in good agreement in comparison with the experiment ($a_{exp} = b_{exp}$ = 4.587 Å, c_{exp} = 2.954 Å and d_{Ti-O} = 1.976 Å) [16]. Four bridges and four cus sites comprise the surface in the x–y plane in Figure 1b. The obtained slab models were set at 15 Å vacuum gaps on each site of the slab in the z-orientation, and the simulated domains were expanded with periodic boundary conditions in Cartesian coordinates.

To imitate the catalytic process of the Equations (1) and (2), the water molecules were, furthermore, released atop the slab at the marked Ti atoms. The initial water adsorbate consisted of the hydroxyl (–OH) ions with an additional hydrogen atom; the hydrogen atom was toward the oxygen of bridge site [17]. Considering the single H_2O adsorbate with monolayer coverage of water [16,37], the surface models from one to four H_2O adsorbed molecules were constructed. Before constructing the models with single Cl adatom structure, optimization had been performed for the slabs with H_2O adsorbate. Finally, the single Cl adatoms would be individually placed to the six initial positions (p_1 to p_6) along the dashed light-blue rectangular line in Figure 1b; Cl adatoms would be placed in six different distances (1.5 Å to 4 Å) between the Cl adatom and the top of slab (this parameter is named "the height" (*h*), Figure 1a). To simplify the combinations of Cl/H_2O/slab surface models, there must be a H_2O adsorbate at p_5 position called H_2O_{Cl} which was utilized to observe the variations of d_{O-H}, as well as to the interaction between Cl adatom, H_2O_{Cl}, and surface. Thus, there were eight types of slabs with H_2O adsorbates in Figure 1c–j. In total, there were 288 initial surface models, consisting of eight variations of slabs with H_2O adsorbates and a Cl adatom with six different heights at six assigned positions.

Practically, the models would usually be obtained to further conduct the AIMD calculations after the structure optimizations. The statistical results of relaxed geometries for our initial surface models are shown in Figure 1k and in Supplementary Figure S2. In brief, the optimized Cl adatom would prefer to locate around the cus sites of surface and place with more waters; the height between Cl adatom and surface TiO_2 was a least 2.5 Å [48]. In contrast, the Cl features illustrated an apparent height of 2 Å above the Ti rows of rutile TiO_2 (110) surface from the STM results [49]. Thus, the initial geometries to be optimized for AIMD consist of surface structures with Cl adatom above the surface and located in the bridge position. Both optimized and non-optimized surface models were

utilized to perform the AIMD for simulating equilibrated configurations in order to achieve the most realistic scenario.

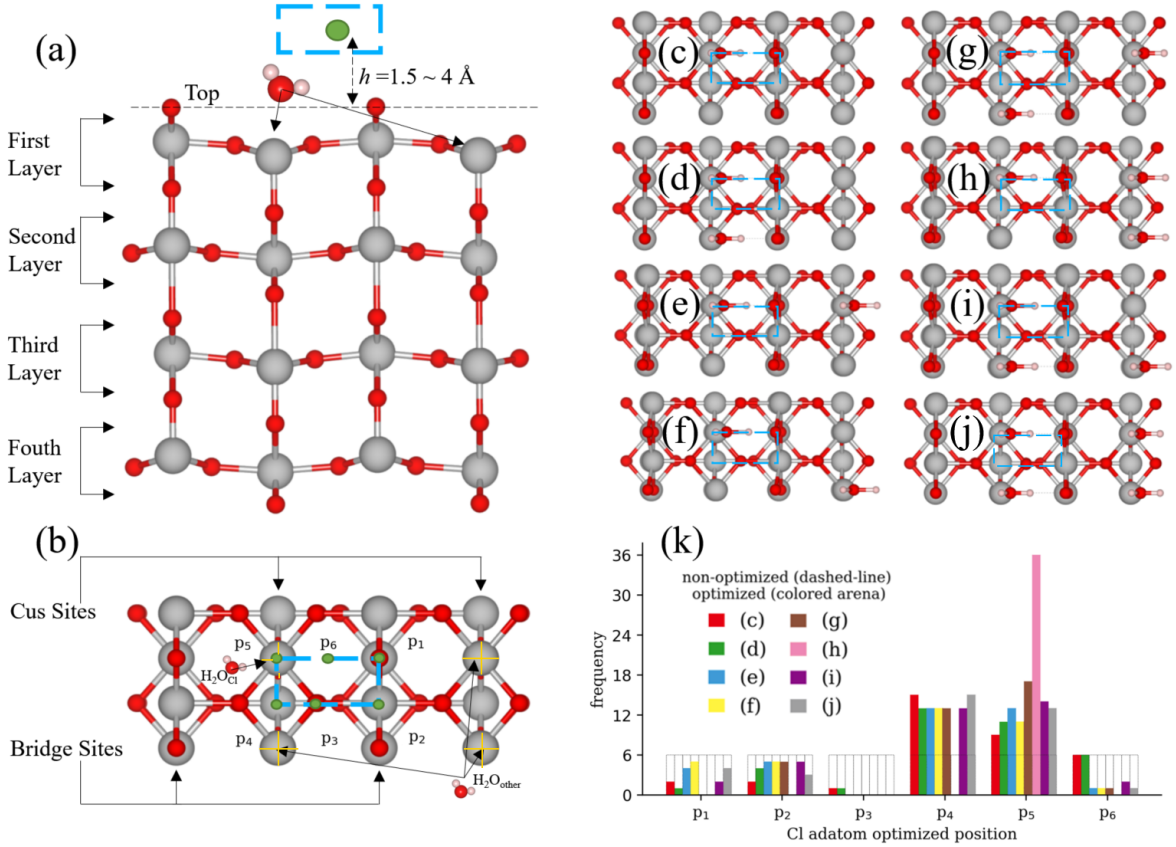

Figure 1. TiO_2 surface models of Cl adatom on the rutile (110) surface with H_2O adsorbate. (**a**) Side view and layer definition of the TiO_2 surface models used in this research; (**b**) top view and adsorption sites atop the slab are defined as cus and bridge sites. The yellow crosses marked on the Ti atoms indicate the positions of H_2O adsorbates. The green spheres represent the initial positions of Cl adatom along the blue dashed rectangular line from p_1 to p_6. H_2O_{Cl} is the water at the p_5 position; other H_2O adsorbates are named H_2O_{other}. This study considers various surface structures of rutile TiO_2 (110) with attached H_2O adsorbate, as depicted in Figure (**c**–**j**). These structures include a surface with one water molecule (**c**), structures with two water molecules (**d**–**f**), three water molecules (**g**–**i**), and a structure with four water molecules (**j**). The statistics of optimized Cl adatom positions are shown in Figure (**k**); the colored bars correspond to the surface structures (**c**–**j**), while the empty black rectangular bars depict the non-optimized Cl adatom position.

3. Results and Discussions

3.1. Ab Initio Molecular Dynamics (AIMD)

For the thermally equilibrated TiO_2 surface models, firstly, AIMD calculations were performed for both optimized and non-optimized initial structures. Posterior to AIMD, the thermalized d_{O-H} of each water is shown in Figure 2. The relationship between the potential energy and d_{O-H} can generally be divided into four regions as d_{O-H} increases from zero to infinity: repulsion, potential energy minimum, attraction, and full bond breaking [50]. Each subgraph in Figure 2 separates these regions into four spaces (I–IV), as described below. Region I, represented by the gray area, corresponds to the repulsion caused by the hydrogen and oxygen being too close. For region II, inside the dashed line, the d_{O-H} distance is considered a bonded situation. Normally, the d_{O-H} corresponding to potential energy minimum is defined as the equilibrium bond length. From the experiments,

the equilibrium bond length of water (r^{exp}_{O-H}) is depending on the phases, temperature, configurations and other parameters, such as 0.9572 Å [51], 0.98 Å, and 1.01 Å [52,53]. For the optimized slabs with H_2Os adsorbate in Figure 1c–j, the average d_{O-H} is 0.978 Å. The cases in the range of region II are not considered as the dissociation. For the cases in region III, represented by the yellow area, the bond lengths meet the criteria for breaking the d_{O-H}, but attractive forces still influence the hydrogen and oxygen. From the AIMD trajectories in the Supplementary Figure S1, the d_{O-H} are mainly oscillated in this region. Therefore, the d_{O-H} in region III are classified to the cases between dissociation and non-dissociation. Besides, Equations (1) and (2) indicated the hydrogens of each water molecule would not be dissociated simultaneously. Thus, the thermalized configurations, inside and closing to the two yellow rectangular areas in region III, would be further studied using ED–TDDFT calculations. When the d_{O-H} distance increases to infinity, the oxygen and hydrogen become two fully dissociated atoms. In this study, 2 Å is set to determine the full dissociation for d_{O-H} in region IV.

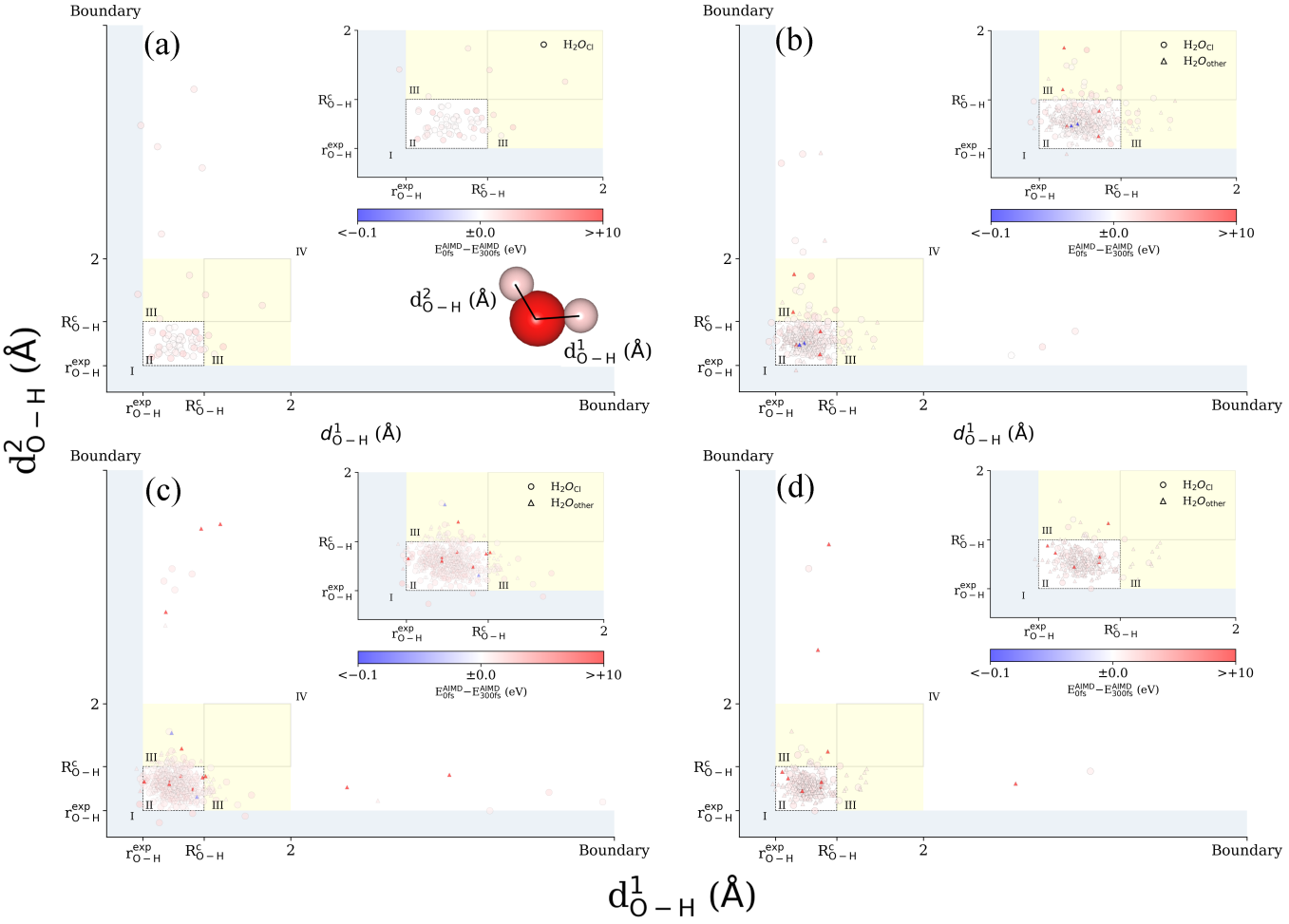

Figure 2. Bond–length (d_{O-H}) distributions for each water molecule correlation to the total energy difference between the initial and final configurations after AIMD. The four diagrams of (**a**–**d**) individually represent the types of rutile (110) surface with one, two, three, or four H_2O adsorbates according to the Figure 1c–j, respectively. The illustration of water bond-lengths is the insets in (**a**). The criteria of bond-breaking are determined by the coordination number cutoff R^C_{O-H} = 1.3 Å [16,37]; the r^{exp}_{O-H} is 0.9572 Å for isolated water molecule in vacuum [51]. The boundary is set to be 10 Å. The insets are the zoom-in view around the criteria of bond-breaking. The energy difference between the initial (0 fs) and the final (300 fs) AIMD state is represented by the colour intensity on blue–red scale.

The vacuum gap between boundaries has been set to 10 Å in order to exclude atoms that are too close to the edge of the simulated domain. Indeed, the configurations, which present the d_{O-H} as larger than the boundary, would not be discussed to be thermalized dissociation. The relationship between kinetic energy, energy barrier, and energy difference during AIMD is analyzed in the Supplementary Figure S3. In short, a strong repulsion would lead to the unreasonable momentum and even destruct the TiO_2 surface models as in the Supplementary Figure S4 when the initial Cl adatom is too close to the surface or H_2O adsorbate corresponding to inappropriate guess. The excess of kinetic energy could also cause the d_{O-H} to become disproportionate, e.g., when the distance between oxygen and hydrogen atoms being tens or even hundreds angstrom. This statement is further supported by the information presented in the Supplementary Figures S3 and S4, which illustrates that, when the Cl adatom is positioned too close to the surface, it acquires a substantial amount of energy that results in the displacement of both the Cl adatom and the H atom away from the surface.

Without consideration of the improper cases for huge momentum, the total energy difference between the initial and the final state for each AIMD path show similar increases for most cases with the increasing H_2O adsorbates on the surface. This results in a situation where more H_2Os are absorbed on the surface with a lower ratio of dissociated cases, as seen in Figure 2. As observed in experiments [54,55], the concentration of chlorine can impact not only the hydrated surface and the amount of adsorption, but also the variations of surface charge and reactivity. Since kinetic and potential energy are limited by temperature, the enhanced energy of each atom is approximately equal to the average energy of the whole system. On the hydrated surface with extra Cl adatom, a single water molecule is more likely to trigger dehydrogenation and form hydroxyl compared to a full coverage of H_2O adsorbates. On the other hand, a higher ratio of Cl adatom to water molecules would cause chlorine to move away from the surface, as seen in the structure optimization in the Supplementary Figure S2. The question remains whether a single Cl adatom can truly react at the interface with low coverage of H_2O adsorbates on the surface. Hence, the concentration of Cl adatoms is not the only concern. The extra deposited chlorine should balance the coverage of H_2O adsorbates and its location on the interface, but investigating this relationship is beyond the scope of the photoexcitation time observed in this study.

Before performing calculations for excited states, we used AIMD to generate equilibrated structures at a given temperature, but not to predict the exact reaction outcome through thermal processes. Interestingly, there are some cases in our AIMD simulations in regions III and IV of Figure 2 that meet the criteria for water splitting defined by Equations (1) or (2), as described in Supplementary Figure S5.

Actually, the trajectories of oscillated d_{O-H} (yellow line) also indicate the analogous behaviors during AIMD in the supplementary S1. The time duration of 300 fs for AIMD in this work is actually not enough to represent the full complicated reactions in comparison with the conventional application of molecule dynamics, which normally set the time scale up to tens or hundreds picosecond for analyzing the surface reactivity [16,37].

In summary, as it follows from AIMD calculations, the Cl adatom plays a role in redistributing the local atomic environment within ultra-fast time and activating water splitting during AIMD. From the perspective of thermal equilibrium, the bond-breaking events of water arise from the momentum. The initial Cl adatom, if located too close to the surface and H_2O adsorbate, tends to move away from the surface due to the high kinetic energy. Besides, the structure optimizations indicate that there is a certain distance between the Cl adatom and the surface with adsorbing water. Additionally, the rapidly oscillated bond lengths indicate the unstable thermalized configurations after AIMD, which should be carefully applied to the initial structures of ED–TDDFT.

3.2. Real-Time Propagation of Time-Dependent Density Functional Theory within Ehrenfest Dynamics (ED–TDDFT)

The photoinduced water dissociation on the pure rutile TiO_2 (110) surface is associated with the electronic states of atomic oxygen sites. The lack of H_2O adsorbate states near the valence band maximum (VBM) edge makes bond-breaking events challenging [17]. It is expected that photoinduced dissociation would be gained from both the improvement of band gap and the extra existing density of state (DOS) for H_2O_{Cl} and chlorine around VBM. The evolution of two photoinduced water dissociation processes is shown in Figure 3. It appears that there are two distinct dissociation processes under investigation. The first process involves the complete dissociation of a water molecule, where the distance between the oxygen and hydrogen atoms (d_{O-H}) is greater than 2 Å. This is illustrated in Figure 3a. The second process involves the dissociation of a water molecule where the hydrogen atom (H_{dis}) remains close to the oxygen atom and oscillates between the dissociated water (O_{water}) and bridge sites (O_{bridge}) on the slab. In this process, the d_{O-H} distance meets the criteria for bond-breaking along the reaction path. This process is shown in Figure 3b. Both processes were investigated using configurations obtained from AIMD simulations. The motions of atoms and the Δn_{ex-gs} were investigated after the excitation for the whole systems. The bottom panels of Figure 3a,b show the initial geometric structures of ED–TDDFT utilized to determine the vertical excitation energy. The DOSes analysis of ground state calculations reveals that the Cl adatom can form states around the VBM edge and improve the band gap performance [56]. In our models, the H_2O_{Cl} in Figure 1b were specifically considered to monitor the DOSes corresponding to the water molecule states around VBM for the ground state calculation, and its first peak of DOS was adopted to the photoexcitation. For both cases in Figure 3, the initial geometries of H_{dis} are almost dissociated from the H_2O_{Cl}. The d_{O-H} of H_{dis} and O_{bridge} in Figure 3b meet the bonding criteria during the reaction. However, the coordination number cutoff R^C_{O-H} does not fully explain why similar initial positions of H_{dis} lead to different final results after excitation.

To get more insights into the mechanisms of photogenerated charge redistribution, the Δn_{ex-gs} is a powerful expression and usually gives unique fingerprints of the localized electronic distributions along the reaction pathways. The variations of isosurfaces can be observed at Δn_{ex-gs} in Figure 4 at assigned moments according to Figure 3. Figure 4a tracks the moment of dissociation at 11.1 fs (O_{water}–H_{dis}), as well as association at 13.5 fs (O_{bridge}–H_{dis}) and 20.9 fs (O_{water}–H^{other}_{water}); Figure 4b monitors the process of oscillated dissociation at 8.6 fs (O_{water}–H_{dis}) and 22.6 fs (O_{bridge}–H_{dis}), as well as association of at 12.9 fs (O_{bridge}–H_{dis}) and 22.9 fs (O_{water}–H_{dis}). At first glance, the Δn_{ex-gs} depletion of O_{water} exists in Figure 4a during the whole reaction, while the behaviors of O_{water} include Δn_{ex-gs} depletion and accumulation in Figure 4b. Additionally, the formation of photogenerated holes can be observed around the oxygen atoms. As for the O_{bridge}, both cases show the Δn_{ex-gs} accumulation around the initial excitation. However, it can be found that the Δn_{ex-gs} accumulation transforms into depletion from 8.6 fs to 12.9 fs in Figure 4b when the H_{dis} is oscillated to the oxygen between the O_{water} and O_{bridge}. As for chlorine, interactions between H_2O_{Cl} are more prevalent in the fully dissociated reaction than the oscillating reaction. The distributions of Δn_{ex-gs} provide abundant charge transitions in detail with the smaller value of isosurfaces. Nonetheless, identifying the exact activities of each element is too complicated. In fact, the Δn_{ex-gs} accumulations or depletion could be incomprehensibly related to the motion of ions. Despite this, the chlorine exhibits more active interaction to the interface and H_2O_{Cl} responds to the obvious coupling between the surrounding atoms from the viewpoint of Δn_{ex-gs}. Nevertheless, predicting the mechanism of spatial confinement and the actual role of chlorine along reaction pathways, particularly the mechanism of charge transfer and atomic dynamics during dissociation, is still a challenging task.

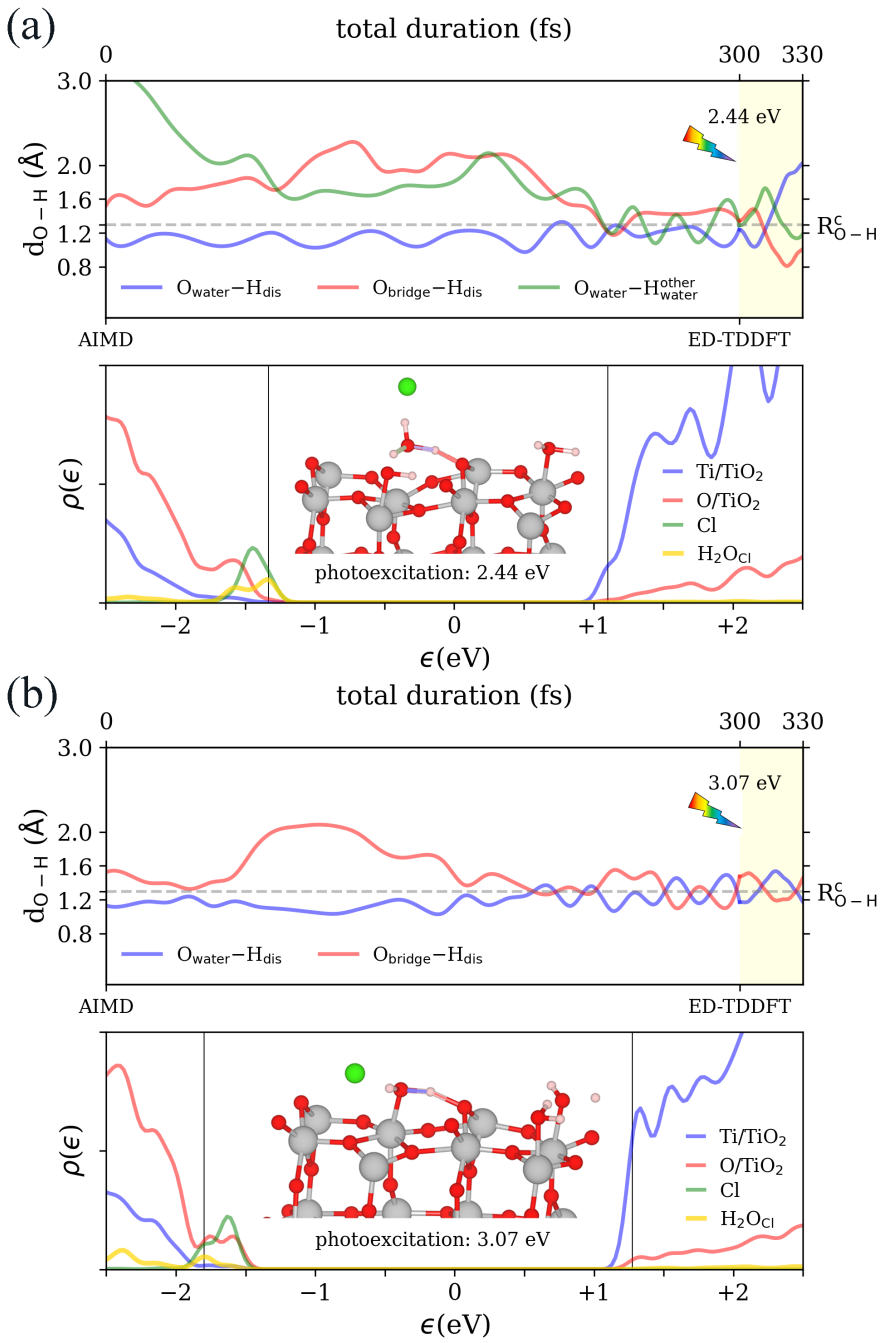

Figure 3. Time evolved O–H bond length (d_{O-H}) for the total duration and density of states (DOS) for determining the excitation energy after AIMD run. The d_{O-H} of (**a**) fully dissociated reaction and (**b**) dissociated hydrogen (H_{dis}) oscillated to the oxygen between the dissociated water (O_{water}) and bridge sites (O_{bridge}) are recorded during AIMD and ED–TDDFT, which are involved in H_2O_{Cl} adsorbate for O_{water}–H_{dis} (blue lines) and O_{bridge}–H_{dis} (red lines). The O_{water}–H^{other}_{water} (green lines) represent that the O_{water} molecule dissociating or associating with hydrogen from another water molecule. The grey dashed lines represent the R^C_{O-H} equal to 1.3 Å. The DOSes corresponding to (**a**,**b**) at the simulation of 300 fs are, respectively, shown in on the bottom panels, and the middle of its band gap is defined as the zero of the energy. The insets in the bottom panels of (**a**,**b**) show the initial geometric structures used for ground state calculations of the DOS. The projections of Ti/TiO_2, O/TiO_2, Cl, and H_2O_{Cl} are colored by blue, red, green and yellow solid lines, respectively. Two vertical black lines around the band gap represent the CBM and designed VB, which relate the energy gap between the CBM and the first peak of H_2O_{Cl}.

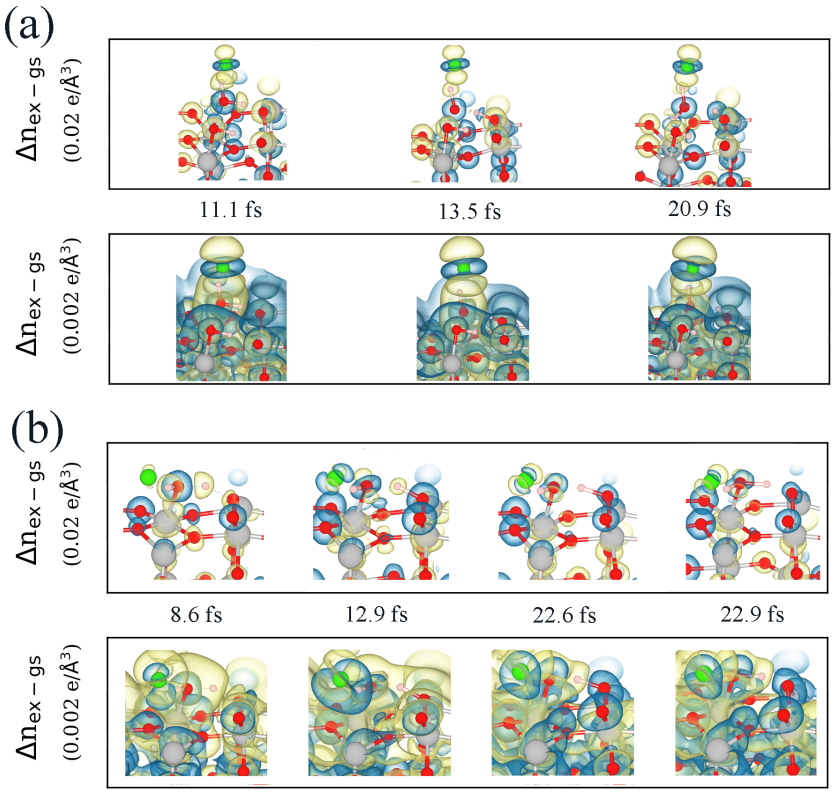

Figure 4. The difference between the total charge densities of the excited states and the ground states (Δn_{ex-gs}) of the surface models at different time steps during the photoexcitation. The geometric configurations are based on Figure 3 for (**a**,**b**), respectively. The Δn_{ex-gs} are expressed by two isosurfaces with value 0.02 (top panels) and 0.002 (bottom panels) e/Å^3, where transparent yellow and blue signify volume of the Δn_{ex-gs} accumulation and depletion, respectively.

Based on the dynamic trajectories (yellow regions) of bond lengths in Figure 3a,b, the evolution of excited states in time during the ED-TDDFT are shown in Figure 5. Because of the ambiguous relation between the Δn_{ex-gs} and dissociation, the localized attraction or repulsion of atomic environments via charge transferring are further analyzed by Hirshfeld charges (q_H) method [57,58] in Figure 5. The differences between the ground (dashed line , without light-driven) state and the excited state (solid line , with light-driven) are clearly illustrated at each sampling time step , which is the other expression to quantify the charge distributions of the reaction pathways with and without light-driven factors for each atomic element. In fact, the variations of geometry would slightly change and cause the transferred q_H of ground state during the time propagations. However, the transferred q_H of the excited state are obviously dominated after excitation. According to Coulomb's law, charges with the same sign repel each other, and charges with opposite signs attract. The motion of H_{dis} is governed by the competition between O_{water} and O_{bridge}. The isosurfaces in Figure 4 can show the Δn_{ex-gs} depletion and accumulation, but the localized q_H value of positive or negative for O_{water} and O_{bridge} has a substantial impact on the dynamical motions concerning the positive charges of H_{dis}.

The driving force for photoinduced water splitting plays a key role in forming hydroxyl ions and dissociated hydrogen. In our models, the Cl adatom on the hydrated TiO_2 surface can form molecule states around the VBM, and the initial excitation causes a charge transition from the VB related to H_2O_{Cl} to the CBM. From the time-dependent charge distributions, the excitation initially triggers the charges of O_{water} to become positively charged q_H within an ultrafast time. This phenomenon initiates the first step of H_2O splitting into hydroxyl and hydrogen due to the repulsion between O_{water} H_{dis}. In the consideration with the fully dissociated reaction in Figure 5a, the responded q_H of O_{bridge}

are more negative than O_{water} in the time of pathways. Therefore, the attraction force from bridge site is larger than the original water molecules, which causes the increment of bond-lengths between O_{water} and H_{dis}, as well as achieves the success of water splitting. In contrast, the H_{dis} is comparably attracted by both the O_{water} and O_{bridge} in Figure 5b. Although both reactions present the obvious increasing positive q_H of O_{water} that repel the H_{dis} after the excitation, the localized q_H transferring reveal the different pathways of transition from the chlorine and surrounding atoms. Indeed, the O_{water} eagerly grabs the negative q_H from the surrounding atoms to sustain the balance. In Figure 5a, the chlorine of fully dissociated reaction picks up more charges from the space and causes the q_H of O_{water} to be not negative enough. To the contrary, the chlorine becomes the donor providing the electron, and, thus, let the total q_H of O_{water} sustain to a negative value approaching the initial condition shown in Figure 5b.

Motivated by the above considerations, the mechanism of Equations (1) and (2) can be reinterpreted. From Equation (1), even if the direct dissociations could be triggered, the lack of intermediate states means that the H_{dis} would oscillate between the O_{water} and O_{bridge}. The effect of electron localization on d-orbitals has an impact on the formation of polarons in titanium, meaning that the charges are trapped around the Ti surroundings and are less transferred or even blocked [17,41–43,45]. Although the q_H of Ti_{water} may fluctuate due to the transfer of neighboring electrons and ions, there is not expected to be a significant transfer of q_H from the surface to the adsorbate. The intermediate states of chlorine and hydronium avoid the direct competition between the O_{water} and O_{bridge}, and they provide buffers for dealing with the q_H transfers. Meanwhile, the photogenerated holes of O_{water} can persist for a longer time. The localized charge transition can be supplied through the charge distribution of intermediate states.

In Figure 4a, the significant change in electron density (Δn_{ex-gs}) is observed in both chlorine and hydrogen regions. The reaction pathways of full dissociation predict a more negative q_H or chlorine after photoexcitation. In turn, the q_H of O_{water} would be positive again due to the charge transferring at 25 fs in Figure 5a. The circumstance reveals another formation of intermediate state, which is the bonding between hydrogen and chlorine. From the spatial confinements, the H_{water} is closer to the Cl adatom. Taking into account that q_H is less negative in the bond of O_{water}, the chlorine has more influence on H_{water}. It is expected that the orbitals of hydrogen and chlorine become coupled, leading to the formation of a bond.

In summary, the presence of a chlorine adatom has a significant impact on the rutile TiO_2 (110)/water interface. The extra chlorine adatom has the potential to facilitate photooxidation to hydroxyl. Our results provide two key insights. Firstly, the mechanistic illustrations clearly demonstrate the influence of attraction and repulsion from the water molecule and the surface and reveal two reaction pathways: fully dissociated reaction and oscillated dissociation. The motions of H_{dis} are dominated by the O_{water} and O_{bridge}. From the Equation (1), the direct dissociation of dehydrogenation cannot avoid the straight competition between the O_{water} and O_{bridge}. Due to the lack of other intermediate states, the lifetime of positive q_H for O_{water} is not long enough to sustain until the fully dissociated reaction, which lets H_{dis} swing from O_{water} to O_{bridge} repeatedly. From Equation (2), the intermediate states of hydronium reconcile why there are more frequent observations of water dissociations of wet surfaces than nearly dry surface used in calculations [16,37]. Our results suggest that the presence of chlorine and hydronium can increase the number of reaction pathways for charge transfer, leading to a positive charge on the water molecule after excitation and ultimately, full dissociation.

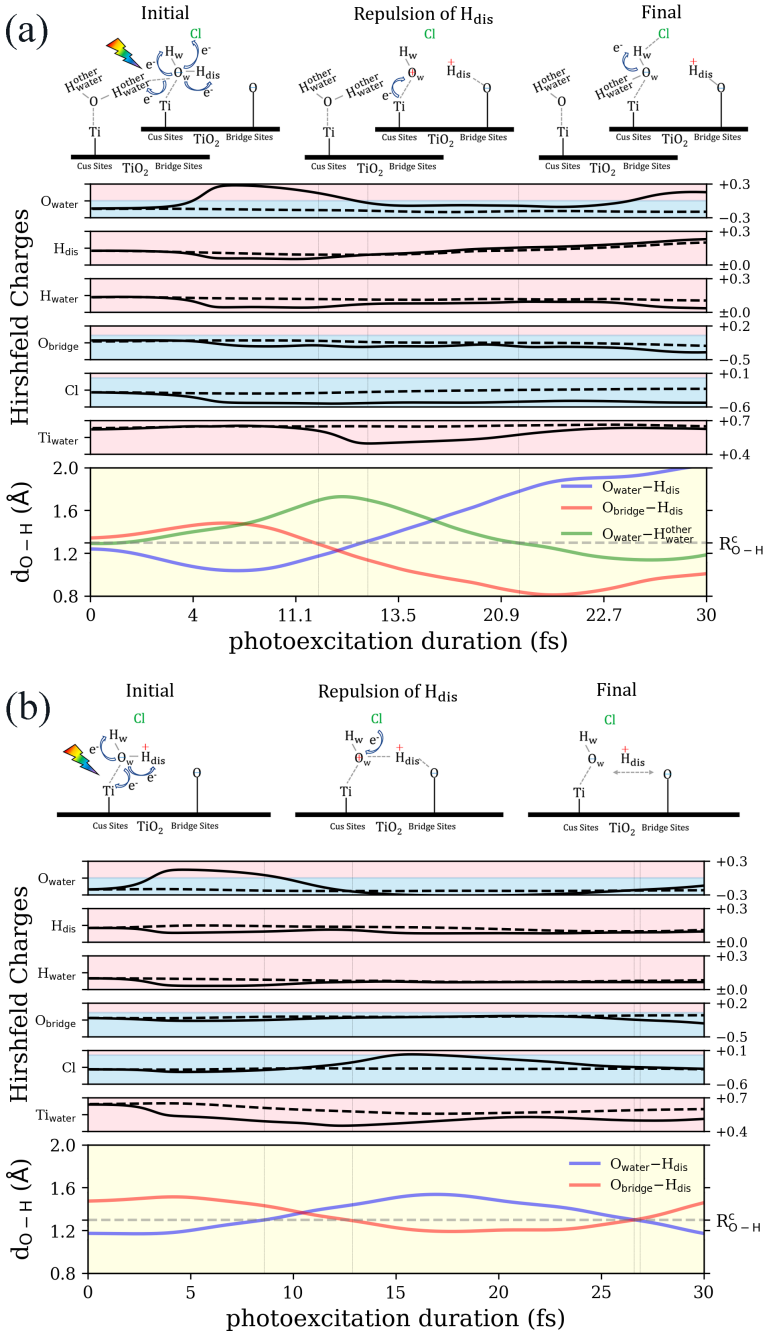

Figure 5. Time evolved O-H bond length (d_{O-H}), Hirshfeld charges (q_H), and a schematic representation of charge transfer during the photoexcitation duration. Panel (**a**) displays the reaction of full dissociation, while panel (**b**) shows the oscillation reaction of dissociated hydrogen, which is the same as shown in Figure 3 (light yellow span). The bottom panels present the time-dependent d_{O-H} along the reaction, and the legends are the same as those in Figure 3a,b, respectively. The middle panels show the time evolution of q_H for different atoms: the titanium nearest to H_2O_{Cl} (Ti_{water}), chlorine (Cl), oxygen of bridge site (O_{bridge}), the hydrogen of H_2O_{Cl} (H_{water}), dissociated hydrogen of H_2O_{Cl} (H_{dis}), and oxygen of H_2O_{Cl} (O_{water}), respectively. On the panels of q_H, the black solid lines (dashed lines) are the q_H of excited states (ground states). The light red (light blue) span is the q_H above (below) zero. The top panels show two illustrations of the bond networks of H_2O_{Cl} and the charge transfer on the surface during the reaction. The red cross represents a localized positive q_H, while the blue minus sign indicates a localized negative q_H. The time instants marked in Figure 4 are indicated within the vertical gray-dotted lines in the illustrations of d_{O-H} and q_H.

Second, the properties of chlorine are not universally positive for all reaction pathways in water-splitting. From a controversial viewpoint, the charge transfer of chlorine is not always advantageous for maintaining the hole of O_{water}. One reason is that chlorine atoms provide charge to hydroxyl groups on the surface and reduce the activity of water-splitting. The other reason is that the accepted charge from O_{water} is confined around the chlorine, causing regions of attractive force induced by O_{water} to be weaker than those induced by O_{bridge}. On the positive side, a Cl adatom close to the hydrated surface can actually generate molecule states around the VBM edge, which triggers a localized photogenerated hole of O_{water} and rapid positive q_H within ultrafast time after initial excitation. The chlorine not only improves the band gap of pure TiO_2, but also is beneficial for the formations of oxygen states on the edge of VBM [48,56]. Additionally, it has been noted that the bonding of H_{water} and chlorine can be found after dissociation, which suggests another possible intermediate state.

4. Conclusions

The first steps for water-splitting, which could be accomplished by the thermal equilibrium from the temperature and atomic environment, as well as the localized charge transferring from the photoexcitation, have been reported via modeling the Cl/H_2O/slab surface models. In conclusion, the chlorine around the surface with H_2O adsorbate could trigger the dehydrogenation of a water molecule from the thermal effect and photoexcitation. Uniting the photoexcitation and thermal dynamics is a huge challenge due to the crossing time scales and different governing equations, which also implies whether the photoinduced dissociations could still be existed from the femtosecond to picosecond. Besides, how to construct the more realistic atomic structures is another challenge to enhance the values of the computational results. Nevertheless, the novelty of this work fulfills the atomic motions and electronic structures with considerations of the photoexcitation and thermal dynamics simultaneously under the circumstance of adding the extra chlorine on the water/TiO_2 interface, which guide the design inspirations of the photocatalytic systems for applying the photoinduced water-splitting.

Supplementary Materials: The following supporting information can be downloaded at: https://www.mdpi.com/article/10.3390/electronicmat4010004/s1, Figure S1: Comparison of d_{O-H} between $U_{Ti}(d) = 0$ eV and $U_{Ti}(d) = 4.2$ eV; Figure S2: Comparison of optimized and non–optimized TiO_2 surface models; Figure S3: Relation between kinetic energy, energy barrier and energy difference during AIMD; Figure S4: Inappropriate initial position of Cl adatom causing destroy the surface during AIMD; Figure S5: Water splitting reaction induced by thermal equilibrium.

Author Contributions: Conceptualization, Y.-P.L., D.B., A.I.P. and S.P.; methodology, Y.-P.L. and S.P.; software, Y.-P.L.; validation, Y.-P.L., D.B., I.I., A.A.P. and S.P.; formal analysis, Y.P.L, D.B., A.I.P. and S.P.; investigation, Y.-P.L.; resources, S.P. and A.I.P.; data curation, Y.-P.L. and S.P.; writing—original draft preparation, Y.-P.L.; writing—review and editing, Y.-P.L., D.B., I.I., V.P., A.A.P., A.I.P. and S.P.; visualization, Y.-P.L.; supervision, D.B. and S.P.; project administration: I.I. and S.P.; funding acquisition: S.P. All authors have read and agreed to the published version of the manuscript.

Funding: This study was financially supported M-ERA.NET project CatWatSplit. Institute of Solid State Physics, University of Latvia, as the Center of Excellence, has received funding from the European Union's Horizon 2020 Framework Program H2020-WIDESPREAD-01-2016-2017-TeamingPhase2 under Grant Agreement No. 739508, project CAMART^2. The calculations were performed at the Latvian SuperCluster (LASC) located in Institute of Solid State Physics, University of Latvia.

Institutional Review Board Statement: Not applicable.

Informed Consent Statement: Not applicable.

Data Availability Statement: The raw/processed data required to reproduce these findings cannot be shared at this time as the data also form a part of an ongoing study.

Conflicts of Interest: The authors declare no conflicts of interest. The funders had no role in the design of the study; in the collection, analyses, or interpretation of data; in the writing of the manuscript, or in the decision to publish the results.

References

1. Zhang, J.; Hu, W.; Cao, S.; Piao, L. Recent progress for hydrogen production by photocatalytic natural or simulated seawater splitting. *Nano Res.* **2020**, *13*, 2313–2322. [CrossRef]
2. Ahmadvand, S.; Abbasi, B.; Azarfar, B.; Elhashimi, M.; Zhang, X.; Abbasi, B. Looking beyond energy efficiency: An applied review of water desalination technologies and an introduction to capillary–driven desalination. *Water* **2019**, *11*, 696. . [CrossRef]
3. Hausmann, J.N.; Schlögl, R.; Menezes, P.W.; Driess, M. Is direct seawater splitting economically meaningful? *Energy Environ. Sci.* **2021**, *14*, 3679–3685. [CrossRef]
4. Gao, M.; Connor, P.K.N.; Ho, G.W. Plasmonic photothermic directed broadband sunlight harnessing for seawater catalysis and desalination. *Energy Environ. Sci.* **2016**, *9*, 3151–3160. [CrossRef]
5. Simamora, A.J.; Chang, F.C.; Wang, H.P.; Yang, T.C.; Wei, Y.L.; Lin, W.K. H_2 fuels from photocatalytic splitting of seawater affected by nano–TiO_2 promoted with CuO and NiO. *Int. J. Photoenergy* **2013**, *2013*, 419182. [CrossRef]
6. Ji, S.M.; Jun, H.; Jang, J.S.; Son, H.C.; Borse, P.H.; Lee, J.S. Photocatalytic hydrogen production from natural seawater. *J. Photochem. Photobiol. A: Chem.* **2007**, *189*, 141–144. [CrossRef]
7. Yang, C.; Qin, J.; Rajendran, S.; Zhang, X.; Liu, R. WS_2 and C–TiO_2 nanorods acting as effective charge separators on g–C_3N_4 to boost visible–light activated hydrogen production from seawater. *ChemSusChem* **2018**, *11*, 4077–4085. [CrossRef]
8. Perović, K.; dela Rosa, F.M.; Kovačić, M.; Kušić, H.; Štangar, U.L.; Fresno, F.; Dionysiou, D.D.; Loncaric Bozic, A. Recent achievements in development of TiO_2-based composite photocatalytic materials for solar driven water purification and water splitting. *Materials* **2020**, *13*, 1338. [CrossRef]
9. Dorosheva, I.; Rempel, A.; Trestsova, M.; Utepova, I.; Chupakhin, O. Synthesis of a TiO_2 Photocatalyst for Dehydrogenative Cross-Coupling of (Hetero) Arenes. *Inorg. Mater.* **2019**, *55*, 155–161. [CrossRef]
10. Serga, V.; Burve, R.; Krumina, A.; Pankratova, V.; Popov, A.I.; Pankratov, V. Study of phase composition, photocatalytic activity, and photoluminescence of TiO_2 with Eu additive produced by the extraction-pyrolytic method. *J. Mater. Res. Technol.* **2021**, *13*, 2350–2360. [CrossRef]
11. Kenmoe, S.; Lisovski, O.; Piskunov, S.; Bocharov, D.; Zhukovskii, Y.F.; Spohr, E. Water adsorption on clean and defective anatase TiO_2 (001) nanotube surfaces: A surface science approach. *J. Phys. Chem. B* **2018**, *122*, 5432–5440. [CrossRef] [PubMed]
12. Dorosheva, I.; Valeeva, A.; Rempel, A.; Trestsova, M.; Utepova, I.; Chupakhin, O. Synthesis and physicochemical properties of nanostructured TiO_2 with enhanced photocatalytic activity. *Inorg. Mater.* **2021**, *57*, 503–510. [CrossRef]
13. Schneider, J.; Matsuoka, M.; Takeuchi, M.; Zhang, J.; Horiuchi, Y.; Anpo, M.; Bahnemann, D.W. Understanding TiO_2 photocatalysis: Mechanisms and materials. *Chem. Rev.* **2014**, *114*, 9919–9986. [CrossRef] [PubMed]
14. Margineda, J.; English, N.J. Dynamical and structural properties of adsorbed water molecules at the TiO_2 rutile–(110) surface: Interfacial hydrogen bonding probed by ab–initio molecular dynamics. *Mol. Phys.* **2020**, *118*, e1725166. [CrossRef]
15. Balzaretti, F.; Gupta, V.; Ciacchi, L.C.; Aradi, B.; Frauenheim, T.; Köppen, S. Water reactions on reconstructed rutile TiO_2: A density functional theory/density functional tight binding approach. *J. Phys. Chem. C* **2021**, *125*, 13234–13246. [CrossRef]
16. Agosta, L.; Brandt, E.G.; Lyubartsev, A.P. Diffusion and reaction pathways of water near fully hydrated TiO_2 surfaces from ab initio molecular dynamics. *J. Chem. Phys.* **2017**, *147*, 024704. [CrossRef]
17. Tritsaris, G.A.; Vinichenko, D.; Kolesov, G.; Friend, C.M.; Kaxiras, E. Dynamics of the photogenerated hole at the rutile TiO_2(110)/water interface: A nonadiabatic simulation study. *J. Phys. Chem. C* **2014**, *118*, 27393–27401. [CrossRef]
18. Sumaria, V.; Krishnamurthy, D.; Viswanathan, V. Quantifying Confidence in DFT Predicted Surface Pourbaix Diagrams and Associated Reaction Pathways for Chlorine Evolution. *ACS Catal.* **2018**, *8*, 9034–9042. [CrossRef]
19. Pham, T.A.; Ping, Y.; Galli, G. Modelling heterogeneous interfaces for solar water splitting. *Nat. Mater.* **2017**, *16*, 401–408. [CrossRef]
20. Ojanperä, A.; Havu, V.; Lehtovaara, L.; Puska, M. Nonadiabatic Ehrenfest molecular dynamics within the projector augmented–wave method. *J. Chem. Phys.* **2012**, *136*, 144103. [CrossRef]
21. Ojanperä, A.; Krasheninnikov, A.V.; Puska, M. Electronic stopping power from first–principles calculations with account for core electron excitations and projectile ionization. *Phys. Rev. B* **2014**, *89*, 035120. [CrossRef]
22. Kolesov, G.; Vinichenko, D.; Tritsaris, G.A.; Friend, C.M.; Kaxiras, E. Anatomy of the photochemical reaction: Excited-state dynamics reveals the C–H acidity mechanism of methoxy photo–oxidation on titania. *J. Phys. Chem. Lett.* **2015**, *6*, 1624–1627. [CrossRef]
23. You, P.; Lian, C.; Chen, D.; Xu, J.; Zhang, C.; Meng, S.; Wang, E. Nonadiabatic dynamics of photocatalytic water splitting on a polymeric semiconductor. *Nano Lett.* **2021**, *21*, 6449–6455. [CrossRef] [PubMed]
24. Lee, Y.; Kolesov, G.; Yao, X.; Kaxiras, E.; Cho, K. Nonadiabatic dynamics of cobalt tricarbonyl nitrosyl for ligand dissociation induced by electronic excitation. *Sci. Rep.* **2021**, *11*, 8997. [CrossRef] [PubMed]
25. You, P.; Chen, D.; Lian, C.; Zhang, C.; Meng, S. First–principles dynamics of photoexcited molecules and materials towards a quantum description. *Wiley Interdiscip. Rev. Comput. Mol. Sci.* **2021**, *11*, e1492. [CrossRef]

26. Kolesov, G.; Grånäs, O.; Hoyt, R.; Vinichenko, D.; Kaxiras, E. Real–time TD–DFT with classical ion dynamics: Methodology and applications. *J. Chem. Theory Comput.* **2016**, *12*, 466–476. [CrossRef]
27. Walter, M.; Häkkinen, H.; Lehtovaara, L.; Puska, M.; Enkovaara, J.; Rostgaard, C.; Mortensen, J.J. Time–dependent density-functional theory in the projector augmented–wave method. *J. Chem. Phys.* **2008**, *128*, 244101. [CrossRef]
28. Gavnholt, J.; Olsen, T.; Engelund, M.; Schiøtz, J. Δ self-consistent field method to obtain potential energy surfaces of excited molecules on surfaces. *Phys. Rev. B* **2008**, *78*, 075441. [CrossRef]
29. Olsen, T.; Gavnholt, J.; Schiøtz, J. Hot–electron–mediated desorption rates calculated from excited–state potential energy surfaces. *Phys. Rev. B* **2009**, *79*, 035403. [CrossRef]
30. Fiorenza, R.; Sciré, S.; D'Urso, L.; Compagnini, G.; Bellardita, M.; Palmisano, L. Efficient H_2 production by photocatalytic water splitting under UV or solar light over variously modified TiO_2–based catalysts. *Int. J. Hydrog. Energy* **2019**, *44*, 14796–14807. [CrossRef]
31. Larsen, A.H.; Mortensen, J.J.; Blomqvist, J.; Castelli, I.E.; Christensen, R.; Dułak, M.; Friis, J.; Groves, M.N.; Hammer, B.; Hargus, C.; et al. The atomic simulation environment—A Python library for working with atoms. *J. Phys. Condens. Matter* **2017**, *29*, 273002. [CrossRef] [PubMed]
32. Bahn, S.R.; Jacobsen, K.W. An object–oriented scripting interface to a legacy electronic structure code. *Comput. Sci. Eng.* **2002**, *4*, 56–66. [CrossRef]
33. Mortensen, J.J.; Hansen, L.B.; Jacobsen, K.W. Real-space grid implementation of the projector augmented wave method. *Phys. Rev. B* **2005**, *71*, 035109. [CrossRef]
34. Enkovaara, J.; Rostgaard, C.; Mortensen, J.J.; Chen, J.; Dułak, M.; Ferrighi, L.; Gavnholt, J.; Glinsvad, C.; Haikola, V.; Hansen, H.A.; et al. Electronic structure calculations with GPAW: A real-space implementation of the projector augmented-wave method. *J. Phys.: Condens. Matter* **2010**, *22*, 253202. [CrossRef]
35. Nocedal, J.; Wright, S.J. *Numerical Optimization: Springer Series in Operations Research and Financial Engineering*; Springer: Cham, Swizterland, 2006.
36. Larsen, A.H.; Vanin, M.; Mortensen, J.J.; Thygesen, K.S.; Jacobsen, K.W. Localized atomic basis set in the projector augmented wave method. *Phys. Rev. B* **2009**, *80*, 195112. [CrossRef]
37. Brandt, E.G.; Agosta, L.; Lyubartsev, A.P. Reactive wetting properties of TiO_2 nanoparticles predicted by ab initio molecular dynamics simulations. *Nanoscale* **2016**, *8*, 13385–13398. [CrossRef]
38. Barca, G.M.J.; Gilbert, A.T.B.; Gill, P.M.W. Simple Models for Difficult Electronic Excitations. *J. Chem. Theory Comput.* **2018**, *14*, 1501–1509. [CrossRef]
39. Ivanov, A.V.; Levi, G.; Jansson, E.A.; Jansson, H. Method for Calculating Excited Electronic States Using Density Functionals and Direct Orbital Optimization with Real Space Grid or Plane-Wave Basis Set. *J. Chem. Theory Comput.* **2021**, *17*, 5034–5049. [CrossRef]
40. Perdew, J.P.; Burke, K.; Ernzerhof, M. Generalized Gradient Approximation Made Simple. *Phys. Rev. Lett.* **1996**, *77*, 3865–3868. [CrossRef]
41. Kowalski, P.M.; Camellone, M.F.; Nair, N.N.; Meyer, B.; Marx, D. Charge localization dynamics induced by oxygen vacancies on the TiO_2(110) Surface. *Phys. Rev. Lett.* **2010**, *105*, 146405. [CrossRef]
42. Morgan, B.J.; Watson, G.W. Intrinsic n-type defect formation in TiO_2: A comparison of rutile and anatase from GGA+U calculations. *J. Phys. Chem. C* **2010**, *114*, 2321–2328. [CrossRef]
43. Vu, N.H.; Le, H.V.; Cao, T.M.; Pham, V.V.; Le, H.M.; Nguyen-Manh, D. Anatase–rutile phase transformation of titanium dioxide bulk material: A DFT+U approach. *J. Phys. Condens. Matter* **2012**, *24*, 405501. [CrossRef]
44. Alghamdi, H.; Idriss, H. Study of the modes of adsorption and electronic structure of hydrogen peroxide and ethanol over TiO_2 rutile (110) surface within the context of water splitting. *Surf. Sci.* **2018**, *669*, 103–113. [CrossRef]
45. Chrétien, S.; Metiu, H. Electronic structure of partially reduced rutile TiO_2(110) surface: Where are the unpaired electrons located? *J. Phys. Chem. C* **2011**, *115*, 4696–4705. [CrossRef]
46. Van der Walt, S.; Colbert, S.C.; Varoquaux, G. The numpy array: A structure for efficient numerical computation. *Comput. Sci. Eng.* **2011**, *13*, 22–30. [CrossRef]
47. Hunter, J.D. Matplotlib: A 2D graphics environment. *Comput. Sci. Eng.* **2007**, *9*, 90–95. [CrossRef]
48. Vogtenhuber, D.; Podloucky, R.; Redinger, J. Ab initio study of atomic Cl adsorption on stoichiometric and reduced rutile TiO_2 (110) surfaces. *Surf. Sci.* **2000**, *454–456*, 369–373. [CrossRef]
49. Vogtenhuber, D.; Podloucky, R.; Redinger, J.; Hebenstreit, E.L.D.; Hebenstreit, W.; Diebold, U. Ab initio and experimental studies of chlorine adsorption on the rutile TiO_2(110) (110) surface. *Phys. Rev. B* **2002**, *65*, 125411. [CrossRef]
50. Enshasy, H.; Al-Haija, Q.A.; Al-Nashr, M.; Al-Muhaisen, S. A schematic design of HHO cell as green energy storage. *Acta Electron. Malays. (AEM)* **2019**, *3*, 9–15. [CrossRef]
51. Huš, M.; Urbic, T. Strength of hydrogen bonds of water depends on local environment. *J. Chem. Phys.* **2012**, *136*, 144305. [CrossRef]
52. Soper, A.K.; Benmore, C.J. Quantum differences between heavy and light water. *Phys. Rev. Lett.* **2008**, *101*, 065502. [CrossRef] [PubMed]
53. Fanourgakis, G.S.; Xantheas, S.S. The bend angle of water in ice Ih and liquid water: The significance of implementing the nonlinear monomer dipole moment surface in classical interaction potentials. *J. Chem. Phys.* **2006**, *124*, 174504. [CrossRef]

54. Li, Y.; He, F.; Peng, S.; Lu, G.; Li, S. Photocatalytic H_2 evolution from NaCl saltwater over $ZnS_{1-x-0.5y}O_x(OH)_y$–ZnO under visible light irradiation. *Int. J. Hydrog. Energy* **2011**, *36*, 10565–10573. [CrossRef]
55. Li, Y.; Gao, D.; Peng, S.; Lu, G.; Li, S. Photocatalytic hydrogen evolution over $Pt/Cd_{0.5}Zn_{0.5}S$ from saltwater using glucose as electron donor: An investigation of the influence of electrolyte NaCl. *Int. J. Hydrog. Energy* **2011**, *36*, 4291–4297. [CrossRef]
56. Tada, K.; Sakata, K.; Yamada, S.; Okazaki, K.; Kitagawa, Y.; Kawakami, T.; Yamanaka, S.; Okumura, M. DFT calculations for Au adsorption onto a reduced TiO_2 (110) surface with the coexistence of Cl. *Mol. Phys.* **2014**, *112*, 365–378. [CrossRef]
57. Hirshfeld, F.L. Bonded–atom fragments for describing molecular charge densities. *Theoret. Chim. Acta* **1977**, *44*, 129–138. [CrossRef]
58. Zhang, Y.; Liu, J.; Zhang, Y.; Bi, Y. Relationship between interatomic electron transfer and photocatalytic activity of TiO_2. *Nano Energy* **2018**, *51*, 504–512. [CrossRef]